






























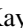



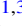








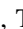

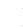





















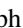












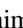





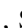







The NANOGrav 15 yr Data Set: Search for Anisotropy in the Gravitational-wave Background

Gabriella Agazie¹ , Akash Anumalapudi¹ , Anne M. Archibald² , Zaven Arzoumanian³, Paul T. Baker⁴ , Bence Bécsey⁵ ,
 Laura Blecha⁶ , Adam Brazier^{7,8} , Paul R. Brook⁹ , Sarah Burke-Spolaor^{10,11} , J. Andrew Casey-Clyde¹² ,
 Maria Charisi¹³ , Shami Chatterjee⁷ , Tyler Cohen¹⁴ , James M. Cordes⁷ , Neil J. Cornish¹⁵ , Fronefield Crawford¹⁶ ,
 H. Thankful Cromartie^{7,6,2} , Kathryn Crowter¹⁷ , Megan E. DeCesar^{18,6,3} , Paul B. Demorest¹⁹ , Timothy Dolch^{20,21} ,
 Brendan Drachler^{22,23} , Elizabeth C. Ferrara^{24,25,26} , William Fiore^{10,11} , Emmanuel Fonseca^{10,11} , Gabriel E. Freedman¹ ,
 Emiko Gardiner²⁷ , Nate Garver-Daniels^{10,11} , Peter A. Gentile^{10,11} , Joseph Glaser^{10,11} , Deborah C. Good^{12,28} ,
 Kayhan Gültekin²⁹ , Jeffrey S. Hazboun⁵ , Ross J. Jennings^{10,11,6,4} , Aaron D. Johnson^{1,30} , Megan L. Jones¹ ,
 Andrew R. Kaiser^{10,11} , David L. Kaplan¹ , Luke Zoltan Kelley²⁷ , Matthew Kerr³¹ , Joey S. Key³² , Nima Laal⁵ ,
 Michael T. Lam^{22,23} , William G. Lamb¹³ , T. Joseph W. Lazio³³, Natalia Lewandowska³⁴ , Tingting Liu^{10,11} ,
 Duncan R. Lorimer^{10,11} , Jing Luo^{35,6,5} , Ryan S. Lynch³⁶ , Chung-Pei Ma^{27,37} , Dustin R. Madison³⁸ ,
 Alexander McEwen¹ , James W. McKee^{39,40} , Maura A. McLaughlin^{10,11} , Natasha McMann¹³ , Bradley W. Meyers^{17,41} ,
 Chiara M. F. Mingarelli^{12,28,42} , Andrea Mitridate⁴³ , Cherry Ng⁴⁴ , David J. Nice⁴⁵ , Stella Koch Ocker⁷ ,
 Ken D. Olum⁴⁶ , Timothy T. Pennucci⁴⁷ , Benetge B. P. Perera⁴⁸ , Nihan S. Pol¹³ , Henri A. Radovan⁴⁹ ,
 Scott M. Ransom⁵⁰ , Paul S. Ray³¹ , Joseph D. Romano⁵¹ , Shashwat C. Sardesai¹ , Ann Schmiedekamp⁵² ,
 Carl Schmiedekamp⁵² , Kai Schmitz⁵³ , Levi Schult¹³ , Brent J. Shapiro-Albert^{10,11,54} , Xavier Siemens^{1,5} ,
 Joseph Simon^{55,6,6} , Magdalena S. Siwek⁵⁶ , Ingrid H. Stairs¹⁷ , Daniel R. Stinebring⁵⁷ , Kevin Stovall¹⁹ ,
 Abhimanyu Susobhanan¹ , Joseph K. Swiggum^{45,6,4} , Stephen R. Taylor¹³ , Jacob E. Turner^{10,11} , Caner Unal^{58,59} ,
 Michele Vallisneri^{30,33} , Sarah J. Vigeland¹ , Haley M. Wahl^{10,11} , Caitlin A. Witt^{60,61} , and Olivia Young^{22,23} 

¹ Center for Gravitation, Cosmology and Astrophysics, Department of Physics, University of Wisconsin–Milwaukee, P.O. Box 413, Milwaukee, WI 53201, USA

² Newcastle University, Newcastle upon Tyne NE1 7RU, UK

³ X-Ray Astrophysics Laboratory, NASA Goddard Space Flight Center, Code 662, Greenbelt, MD 20771, USA

⁴ Department of Physics and Astronomy, Widener University, One University Place, Chester, PA 19013, USA

⁵ Department of Physics, Oregon State University, Corvallis, OR 97331, USA

⁶ Physics Department, University of Florida, Gainesville, FL 32611, USA

⁷ Cornell Center for Astrophysics and Planetary Science and Department of Astronomy, Cornell University, Ithaca, NY 14853, USA

⁸ Cornell Center for Advanced Computing, Cornell University, Ithaca, NY 14853, USA

⁹ Institute for Gravitational Wave Astronomy and School of Physics and Astronomy, University of Birmingham, Edgbaston, Birmingham B15 2TT, UK

¹⁰ Department of Physics and Astronomy, West Virginia University, P.O. Box 6315, Morgantown, WV 26506, USA

¹¹ Center for Gravitational Waves and Cosmology, West Virginia University, Chestnut Ridge Research Building, Morgantown, WV 26505, USA

¹² Department of Physics, University of Connecticut, 196 Auditorium Road, U-3046, Storrs, CT 06269-3046, USA

¹³ Department of Physics and Astronomy, Vanderbilt University, 2301 Vanderbilt Place, Nashville, TN 37235, USA; nihan.pol@nanograv.org

¹⁴ Department of Physics, New Mexico Institute of Mining and Technology, 801 Leroy Place, Socorro, NM 87801, USA

¹⁵ Department of Physics, Montana State University, Bozeman, MT 59717, USA

¹⁶ Department of Physics and Astronomy, Franklin & Marshall College, P.O. Box 3003, Lancaster, PA 17604, USA

¹⁷ Department of Physics and Astronomy, University of British Columbia, 6224 Agricultural Road, Vancouver, BC V6T 1Z1, Canada

¹⁸ George Mason University, Fairfax, VA 22030, USA

¹⁹ National Radio Astronomy Observatory, 1003 Lopezville Road, Socorro, NM 87801, USA

²⁰ Department of Physics, Hillsdale College, 33 E. College Street, Hillsdale, MI 49242, USA

²¹ Eureka Scientific, 2452 Delmer Street, Suite 100, Oakland, CA 94602-3017, USA

²² School of Physics and Astronomy, Rochester Institute of Technology, Rochester, NY 14623, USA

²³ Laboratory for Multiwavelength Astrophysics, Rochester Institute of Technology, Rochester, NY 14623, USA

²⁴ Department of Astronomy, University of Maryland, College Park, MD 20742, USA

²⁵ Center for Research and Exploration in Space Science and Technology, NASA/GSFC, Greenbelt, MD 20771, USA

²⁶ NASA Goddard Space Flight Center, Greenbelt, MD 20771, USA

²⁷ Department of Astronomy, University of California, Berkeley, 501 Campbell Hall #3411, Berkeley, CA 94720, USA

²⁸ Center for Computational Astrophysics, Flatiron Institute, 162 5th Avenue, New York, NY 10010, USA

²⁹ Department of Astronomy and Astrophysics, University of Michigan, Ann Arbor, MI 48109, USA

³⁰ Division of Physics, Mathematics, and Astronomy, California Institute of Technology, Pasadena, CA 91125, USA

³¹ Space Science Division, Naval Research Laboratory, Washington, DC 20375-5352, USA

³² University of Washington Bothell, 18115 Campus Way NE, Bothell, WA 98011, USA

³³ Jet Propulsion Laboratory, California Institute of Technology, 4800 Oak Grove Drive, Pasadena, CA 91109, USA

³⁴ Department of Physics, State University of New York at Oswego, Oswego, NY 13126, USA

³⁵ Department of Astronomy & Astrophysics, University of Toronto, 50 Saint George Street, Toronto, ON M5S 3H4, Canada

³⁶ Green Bank Observatory, P.O. Box 2, Green Bank, WV 24944, USA

³⁷ Department of Physics, University of California, Berkeley, CA 94720, USA

³⁸ Department of Physics, University of the Pacific, 3601 Pacific Avenue, Stockton, CA 95211, USA

³⁹ E.A. Milne Centre for Astrophysics, University of Hull, Cottingham Road, Kingston-upon-Hull HU6 7RX, UK

⁴⁰ Centre of Excellence for Data Science, Artificial Intelligence and Modelling (DAIM), University of Hull, Cottingham Road, Kingston-upon-Hull HU6 7RX, UK

⁴¹ International Centre for Radio Astronomy Research, Curtin University, Bentley, WA 6102, Australia

⁴² Department of Physics, Yale University, New Haven, CT 06520, USA

⁴³ Deutsches Elektronen-Synchrotron DESY, Notkestr. 85, D-22607 Hamburg, Germany

⁴⁴ Dunlap Institute for Astronomy and Astrophysics, University of Toronto, 50 St. George Street, Toronto, ON M5S 3H4, Canada

⁴⁵ Department of Physics, Lafayette College, Easton, PA 18042, USA

⁴⁶ Institute of Cosmology, Department of Physics and Astronomy, Tufts University, Medford, MA 02155, USA

⁴⁷ Institute of Physics and Astronomy, Eötvös Loránd University, Pázmány P.s. 1/A, 1117 Budapest, Hungary⁴⁸ Arecibo Observatory, HC3 Box 53995, Arecibo, PR 00612, USA⁴⁹ Department of Physics, University of Puerto Rico, Mayagüez, PR 00681, USA⁵⁰ National Radio Astronomy Observatory, 520 Edgemont Road, Charlottesville, VA 22903, USA⁵¹ Department of Physics, Texas Tech University, Box 41051, Lubbock, TX 79409, USA⁵² Department of Physics, Penn State Abington, Abington, PA 19001, USA⁵³ Institute for Theoretical Physics, University of Münster, D-48149 Münster, Germany⁵⁴ Giant Army, 915A 17th Avenue, Seattle WA 98122, USA⁵⁵ Department of Astrophysical and Planetary Sciences, University of Colorado, Boulder, CO 80309, USA⁵⁶ Center for Astrophysics, Harvard University, 60 Garden Street, Cambridge, MA 02138, USA⁵⁷ Department of Physics and Astronomy, Oberlin College, Oberlin, OH 44074, USA⁵⁸ Department of Physics, Ben-Gurion University of the Negev, Be'er Sheva 84105, Israel⁵⁹ Feza Gursey Institute, Bogazici University, Kandilli, 34684, Istanbul, Turkey⁶⁰ Center for Interdisciplinary Exploration and Research in Astrophysics (CIERA), Northwestern University, Evanston, IL 60208, USA⁶¹ Adler Planetarium, 1300 S. DuSable Lake Shore Drive, Chicago, IL 60605, USA

Received 2023 July 1; revised 2023 August 18; accepted 2023 August 23; published 2023 October 5

Abstract

The North American Nanohertz Observatory for Gravitational Waves (NANOGrav) has reported evidence for the presence of an isotropic nanohertz gravitational-wave background (GWB) in its 15 yr data set. However, if the GWB is produced by a population of inspiraling supermassive black hole binary (SMBHB) systems, then the background is predicted to be anisotropic, depending on the distribution of these systems in the local Universe and the statistical properties of the SMBHB population. In this work, we search for anisotropy in the GWB using multiple methods and bases to describe the distribution of the GWB power on the sky. We do not find significant evidence of anisotropy. By modeling the angular power distribution as a sum over spherical harmonics (where the coefficients are not bound to always generate positive power everywhere), we find that the Bayesian 95% upper limit on the level of dipole anisotropy is $(C_{l=1}/C_{l=0}) < 27\%$. This is similar to the upper limit derived under the constraint of positive power everywhere, indicating that the dipole may be close to the data-informed regime. By contrast, the constraints on anisotropy at higher spherical-harmonic multipoles are strongly prior dominated. We also derive conservative estimates on the anisotropy expected from a random distribution of SMBHB systems using astrophysical simulations conditioned on the isotropic GWB inferred in the 15 yr data set and show that this data set has sufficient sensitivity to probe a large fraction of the predicted level of anisotropy. We end by highlighting the opportunities and challenges in searching for anisotropy in pulsar timing array data.

Unified Astronomy Thesaurus concepts: [Gravitational waves \(678\)](#); [Gravitational wave astronomy \(675\)](#); [Supermassive black holes \(1663\)](#); [Pulsars \(1306\)](#)

1. Introduction

Using 67 pulsars from its 15 yr data set (Agazie et al. 2023a), the North American Nanohertz Observatory for Gravitational Waves (NANOGrav; McLaughlin 2013; Ransom et al. 2019) has reported $\sim 3\sigma$ – 4σ evidence for a gravitational-wave background (GWB) in the frequency range ~ 2 – 30 nHz (Agazie et al. 2023b, hereafter [NG15gwb](#)). This statistical significance is based on searching for the presence of a distinctive pattern of correlated timing deviations imprinted on otherwise-independent millisecond pulsars. These rotating neutron stars emit beams of radio waves that can intersect our line of sight every rotational period, registering pulses in radio telescopes. The regularity of their rotation and the stability of their epoch-averaged radio pulse profiles allow pulsars to be used as timekeepers with which we can build highly accurate models of their rotation, position, proper motion, binary dynamics (where appropriate), and even the

properties of the intervening interstellar medium through which the radio pulses must travel. Beyond being extraordinary objects in their own right, the timing stability of pulsars makes them excellent tools to study dynamic spacetime.

A gravitational wave (GW) propagating between a pulsar and the Earth will cause a change in the proper length of the photon path, leading to deviations from expected pulse times of arrival (TOAs) that depend on the Earth–pulsar–GW geometry (Estabrook & Wahlquist 1975; Sazhin 1978; Detweiler 1979). For an all-sky stochastic background of GWs, the net timing signature on a given pulsar may appear as a source of random noise with excess power on longer timescales (Phinney 2001). This is challenging to disentangle from other sources of noise such as intrinsic long-timescale pulsar rotational instabilities, or long-timescale variations in the properties of the interstellar medium (see, e.g., Agazie et al. 2023c and references therein). Yet with Earth as the common endpoint of all pulsar observations, the result of correlating the timing deviations between pairs of pulsars in a pulsar timing array (PTA) leads to an expected pattern that is akin to the overlap reduction function (ORF) of other GW detectors. For an isotropic GWB, this pattern is a quasi-quadrupolar signature that depends only on the angular separation of pulsars on the sky, known as the Hellings–Downs (HD) curve (Hellings & Downs 1983). For anisotropic GWBs, this signature takes a different form (e.g., Mingarelli et al. 2013).

The HD curve is used as a template when cross-correlating pulsar timing observations in detection statistics and for

⁶² NASA Hubble Fellowship: Einstein Postdoctoral Fellow.⁶³ Resident at the Naval Research Laboratory, Washington, DC 20375, USA.⁶⁴ NANOGrav Physics Frontiers Center Postdoctoral Fellow.⁶⁵ Deceased.⁶⁶ NSF Astronomy and Astrophysics Postdoctoral Fellow.

inferring the spectral properties of the GWB. It can be shown that in addition to arising due to an isotropic GWB, the HD curve is also the limiting case of binning pairwise correlations for an infinite number of pulsars due to an individual GW signal (Cornish & Sesana 2013; Allen 2023). Therefore, despite the fact that production-level PTA pipelines use unbinned correlation data for inference, the HD curve has been shown to be an effective template for initial detection of the GWB that may nevertheless be anisotropic (Cornish & Sesana 2013; Cornish & Sampson 2016; Taylor et al. 2020; Bécsy et al. 2022; Allen 2023). Indeed, NANOGrav’s evidence for a GWB is based on the statistical significance of cross-correlations matching the HD curve versus the absence of any cross-correlations. Via a range of frequentist and Bayesian analyses that employed various simulations and data-augmentation techniques (Cornish & Sampson 2016; Taylor et al. 2017; Meyers et al. 2023; Vallisneri et al. 2023), NANOGrav constructed statistical background distributions for the significance of HD cross-correlations, resulting in a false-alarm probability of $\sim 5 \times 10^{-5} - 10^{-3}$ ($\sim 3\sigma - 4\sigma$).

While the source of the GWB is not known for certain, one potential source is a population of inspiraling supermassive black hole binaries (SMBHBs) with masses $10^8 - 10^{10} M_\odot$, whose superposition of quasi-monochromatic GW signals manifests as a stochastic background in our PTA. The inferred demographics and dynamics of such SMBHBs are studied in Agazie et al. (2023d). Other processes from the early Universe may contribute to the GWB (see, e.g., Afzal et al. 2023 and references therein); however, an expected outcome of an SMBHB-dominated GWB is the presence of signal anisotropy, either through the clustering of host galaxies or Poisson fluctuations in GW source properties (Mingarelli et al. 2017). GWB anisotropy is often described in terms of the angular power spectrum, wherein the GWB directional power map is decomposed on a spherical-harmonic basis with associated coefficients, and then summarized with $C_l = \sum_{m=-l}^l |c_{lm}|^2 / (2l + 1)$. Estimates of GWB anisotropy from analytic and Monte Carlo population studies produce angular power spectra where $(C_{l>0} / C_{l=0}) \lesssim 20\%$ (Mingarelli et al. 2013, 2017; Taylor & Gair 2013). Recent work by Sato-Polito & Kamionkowski (2023) also demonstrates the importance of high-frequency PTA sensitivity as a means of using anisotropy to probe details of the SMBHB population.

A variety of techniques have been developed to model and infer GWB anisotropy with PTA data, with broad similarities to how such searches are carried out in ground-based detectors (e.g., Allen & Ottewill 1997; Ballmer 2006; Thrane et al. 2009; Renzini & Contaldi 2018; Payne et al. 2020; Essick et al. 2023), and in plans for future space-borne detectors like LISA (e.g., Cornish 2001; Contaldi et al. 2020; Banagiri et al. 2021; Bartolo et al. 2022). Differences arise mostly through the choice of basis on which to express the angular power distribution. Taylor & Gair (2013) developed the first Bayesian PTA pipeline for GWB anisotropy by expressing the angular power as a linear expansion of weighted spherical harmonics. The space of spherical-harmonic coefficients was bounded by a prior requiring that the GWB power be positive everywhere, which was assessed via rejection. The spherical-harmonic basis approach was fully generalized by Gair et al. (2014), who computed an analytic form for ORF basis functions of any $\{lm\}$. Rather than imposing positivity via rejection, a more elegant approach was developed almost simultaneously for

ground-based (Payne et al. 2020), space-borne (Banagiri et al. 2021), and PTA (Taylor et al. 2020) anisotropy searches through which the *square root* of the GWB power was first expressed on a spherical-harmonic basis, thereby naturally imposing positive behavior on the GWB itself. Other techniques have been adapted from CMB analyses to map the polarization content of the GWB (Gair et al. 2014; Kato & Soda 2016; Belgacem & Kamionkowski 2020; Liu & Ng 2022; Sato-Polito & Kamionkowski 2022), although these have yet to be applied to real data. Finally, techniques using data-driven bases for anisotropy modeling show promise; by computing eigen-skies of the noise-weighted PTA response map, the GWB power distribution can be efficiently built from a compact number of basis terms (Cornish & van Haasteren 2014; Ali-Haïmoud et al. 2020, 2021).

The only dedicated PTA search for GWB anisotropy before now was performed by the European Pulsar Timing Array collaboration (Kramer & Champion 2013) using six high-quality pulsars (Taylor et al. 2015). With only 15 distinct pulsar pair combinations, the prospects were limited for detecting anisotropy. They found that the Bayesian 95% upper limit on the characteristic strain in higher spherical-harmonic multipoles—defined as $A_{\text{GWB}}(C_l/4\pi)^{1/4}$ —was $\lesssim 40\%$ of the $l = 0$ amplitude. However, this is almost entirely due to prior constraints enforcing a positive angular power distribution for the GWB, which limited the level of power in higher multipoles with respect to $l = 0$. Almost by definition, data-informed constraints on GWB anisotropy require at least as many pulsars as are necessary for initial evidence of inter-pulsar correlations. It is only now that PTAs have reached this threshold, which motivates the search here.

This Letter is organized as follows. In Section 2 we discuss our methods for describing and searching for GWB anisotropy in the NANOGrav 15 yr data set, including basis choices, and details of our Bayesian and frequentist pipelines. Our results are described in Section 3, followed by a discussion in Section 4 that places these results in context using GWB anisotropy estimates from many realizations of SMBHB populations that were generated with NANOGrav’s `holodeck` simulation software. We conclude and consider future prospects in Section 5.

2. Methods

We search for anisotropy in the GWB by using information from the full set of inter-pulsar correlations (i.e., autocorrelations and cross-correlations) within a Bayesian analysis, as well as only cross-correlations within a frequentist framework. The search for anisotropy using all correlations is performed with the standard PTA Bayesian pipeline that is described in `NG15gwb`, with suitable modifications to account for anisotropy in the GWB. However, since this pipeline is slow for evaluating models with inter-pulsar correlations, we also perform a faster cross-correlation search using a frequentist approach based on the methods developed in Pol et al. (2022). In the following, we discuss the formalism for modeling GWB anisotropy in PTA data, followed by a description of our various analysis pipelines.

2.1. Overlap Reduction Function and the GWB Power

For any PTA with N_{psr} pulsars, the total number of correlations is $N_{\text{tc}} = N_{\text{psr}}(N_{\text{psr}} + 1)/2$, of which there are

$N_{ac} = N_{psr}$ autocorrelations and $N_{cc} = N_{psr}(N_{psr} - 1)/2$ cross-correlations. The angular dependence of these measured correlations on the distribution of GWB power is described by the ORF (Flanagan 1993; Mingarelli et al. 2013; Taylor & Gair 2013; Gair et al. 2014; Taylor et al. 2020), which for a Gaussian, stationary GWB can be written as

$$\Gamma_{ab} \propto \int_{S^2} d^2\hat{\Omega} P(\hat{\Omega}) [\mathcal{F}^+(\hat{p}_a, \hat{\Omega}) \mathcal{F}^+(\hat{p}_b, \hat{\Omega}) + \mathcal{F}^\times(\hat{p}_a, \hat{\Omega}) \mathcal{F}^\times(\hat{p}_b, \hat{\Omega})], \quad (1)$$

where a, b are index pulsars; $P(\hat{\Omega})$ is the power of the GWB in direction $\hat{\Omega}$, normalized such that $\int_{S^2} d^2\hat{\Omega} P(\hat{\Omega}) = 1$; and $\mathcal{F}^A(\hat{p}, \hat{\Omega})$ is the antenna response of a pulsar in the unit-vector direction \hat{p}_a to each GW polarization $A \in [+, \times]$, defined such that

$$\mathcal{F}^A(\hat{p}, \hat{\Omega}) = \frac{1}{2} \frac{\hat{p}^i \hat{p}^j}{1 - \hat{\Omega} \cdot \hat{p}} e_{ij}^A(\hat{\Omega}), \quad (2)$$

where $e_{ij}^A(\hat{\Omega})$ are polarization basis tensors and (i, j) are spatial indices. Note that unlike ground- and space-based GW detectors, the GW-frequency dependence in the ORF can be factored out in the PTA regime, and we use the ORF to represent the angular dependence of the correlations (e.g., Romano & Cornish 2017). If $P(\hat{\Omega}) = 1, \forall \hat{\Omega}$, Equation (1) is proportional to the HD curve.

The integral in Equation (1) can be rewritten as a sum over equal-area pixels (Gair et al. 2014; Taylor et al. 2020) indexed by k :

$$\Gamma_{ab} \propto \sum_k P_k [\mathcal{F}_{a,k}^+ \mathcal{F}_{b,k}^+ + \mathcal{F}_{a,k}^\times \mathcal{F}_{b,k}^\times] \Delta\hat{\Omega}_k. \quad (3)$$

To model GWB anisotropy and compute the ORF, we must choose an appropriate basis on the 2-sphere to represent the GWB power. Here we model the GWB angular power dependence using a spherical-harmonic basis (Mingarelli et al. 2013; Taylor & Gair 2013; Gair et al. 2014; Taylor et al. 2015) and a pixel basis (Cornish & van Haasteren 2014).

2.1.1. Radiometer Pixel Basis

In the radiometer pixel basis (Ballmer 2006; Mitra et al. 2008), the sky is divided into equal-area pixels using HEALPix (Górski et al. 2005):

$$P(\hat{\Omega}) = \sum_{\hat{\Omega}'} P_{\hat{\Omega}'} \delta^2(\hat{\Omega}, \hat{\Omega}'), \quad (4)$$

such that the ORF for a given independently modeled pixel is

$$\Gamma_{ab, \hat{\Omega}} \propto P_{\hat{\Omega}} [\mathcal{F}_{a, \hat{\Omega}}^+ \mathcal{F}_{b, \hat{\Omega}}^+ + \mathcal{F}_{a, \hat{\Omega}}^\times \mathcal{F}_{b, \hat{\Omega}}^\times] \Delta\hat{\Omega}. \quad (5)$$

The number of pixels on the sky is set by $N_{pix} = 12N_{side}^2$, where N_{side} defines the tessellation of the HEALPix sky (Górski et al. 2005). For PTAs, the rule of thumb is to have $N_{pix} \leq N_{cc}$ when counting pieces of information (Romano & Cornish 2017). Given that N_{side} needs to be a power of 2 (Zonca et al. 2019), this imposes a choice of $N_{side} = 8$ for the 15 yr data set with its 67 pulsars, resulting in an angular resolution of $\approx 7^\circ.3$. This basis is ideally suited for detecting widely separated point sources, since we assume that the power between any two neighboring pixels is not correlated.

2.1.2. Spherical-harmonic and Square-root Spherical-harmonic Basis

In the spherical-harmonic basis (Allen & Ottewill 1997), GWB power is written as a linear expansion over the spherical-harmonic functions, which form an orthonormal basis on the 2-sphere, such that

$$P(\hat{\Omega}) = \sum_{l=0}^{\infty} \sum_{m=-l}^l c_{lm} Y_{lm}(\hat{\Omega}), \quad (6)$$

where Y_{lm} are the real-valued spherical harmonics. Without prior restrictions or model regularization on the coefficients c_{lm} , the linear spherical-harmonic basis allows the GWB power to assume negative values, which is an unphysical model of the GWB. We can address this problem by instead modeling the square root of the GWB power, $P(\hat{\Omega})^{1/2}$, rather than the power itself. This technique was introduced in a Bayesian context in Payne et al. (2020) for LIGO, Banagiri et al. (2021) for LISA, and Taylor et al. (2020) for PTAs, while Pol et al. (2022) applied this method in a frequentist context for PTAs. The square root of the power can be decomposed onto the spherical-harmonic basis

$$P(\hat{\Omega}) = [P(\hat{\Omega})^{1/2}]^2 = \left[\sum_{L=0}^{\infty} \sum_{M=-L}^L b_{LM} Y_{LM}(\hat{\Omega}) \right]^2, \quad (7)$$

where Y_{LM} are the real-valued spherical harmonics and b_{LM} are the search coefficients. Banagiri et al. (2021) showed that the search coefficients in the square-root spherical-harmonic basis can be related to the coefficients in the linear basis via

$$c_{lm} = \sum_{LM} \sum_{L'M'} b_{LM} b_{L'M'} \beta_{lm}^{LM, L'M'}, \quad (8)$$

where $\beta_{lm}^{LM, L'M'}$ is defined as

$$\beta_{lm}^{LM, L'M'} = \sqrt{\frac{(2L+1)(2L'+1)}{4\pi(2l+1)}} C_{LM, L'M'}^{lm} C_{L0, L'0}^{l0}, \quad (9)$$

with $C_{LM, L'M'}^{lm}$ being Clebsch–Gordon coefficients. This approach imposes control on the spherical-harmonic coefficients to inhibit the proposal of GWB power distributions with negative regions.

We quantify our results from the spherical-harmonic basis in terms of C_l , which is the squared angular power in each multipole mode l ,

$$C_l = \frac{1}{2l+1} \sum_{m=-l}^l |c_{lm}|^2. \quad (10)$$

C_l is thus a measure of the amplitude of the statistical fluctuations in the angular power of the GWB at scales $\theta = 180^\circ/l$. An isotropic GWB will only have power in the $l=0$ multipole (typically referred to as the monopole), while an anisotropic GWB will have power at higher- l multipoles. As shown in Boyle (2012), the diffraction limit defines the highest multipole, l_{max} , that can be probed in an anisotropic search, which for PTAs scales as $l_{max} \sim \sqrt{N_{psr}}$ (Romano & Cornish 2017), and is $l_{max} \approx 8$ for the NANOGrav 15 yr data set, giving a maximum angular resolution of $\theta = 22.5^\circ$, which is approximately 3 times larger than the resolution of the radiometer pixel basis. Thus, the spherical-harmonic and

radiometer pixel bases are probing anisotropies on large and small angular scales, respectively.

2.2. Bayesian Analysis Pipeline

The Bayesian pipeline is designed to use the full correlation data available to PTAs, i.e., both the spatial auto- and cross-correlations between pulsars in the array (Taylor et al. 2020). Assuming an unpolarized, wide-sense stationary Gaussian GWB, the ORF from Equation (3) can be rewritten in matrix form (Taylor et al. 2020):

$$\Gamma_{ab} = [\mathbf{F}\mathbf{P}\mathbf{F}^T]_{ab}, \quad (11)$$

where \mathbf{P} is a diagonal matrix of size $2N_{\text{pix}}$ describing the GWB power in each polarization for each pixel, and \mathbf{F} represents the PTA signal response matrix of size $N_{\text{psr}} \times 2N_{\text{pix}}$, which can be split into Earth and pulsar term contributions as

$$\begin{aligned} F_{\{a,k,A\}}^E &= \sqrt{\frac{3}{2}} \frac{\mathcal{F}^A(\hat{p}_a, \hat{\Omega}_k)}{N_{\text{pix}}} \\ F_{\{a,k,A\}}^P &= F_{\{a,k,A\}}^E e^{-2\pi i f L_a (1 - \hat{\Omega}_k \hat{p}_a)/c}, \end{aligned} \quad (12)$$

where f is the GW frequency, L_a is the distance to pulsar a , sky pixels are indexed by k , and GW polarization is labeled by $A \in [+, \times]$. Since the distance to pulsars is approximately parsecs or more, the Earth and pulsar term components are numerically orthogonal due to the rapid oscillation of the pulsar term across the sky (Mingarelli & Sidery 2014; Mingarelli & Mingarelli 2018; Taylor et al. 2020). Thus, the pulsar term contribution to the ORF is effectively diagonal, such that

$$\Gamma_{ab} = (1 + \delta_{ab})[\mathbf{F}^E\mathbf{P}\mathbf{F}^{E,T}]_{ab}, \quad (13)$$

where the GWB power matrix \mathbf{P} can be expressed in any convenient basis, since the PTA signal response matrices sandwiching it are performing the necessary sky integral through a numerical sum over pixels.

The Bayesian pipeline is constructed identically to the one described in NG15gwb. Given an ORF Γ_{ab} , the GWB cross-power spectrum can be written as $\Phi_{ab,j} = \Gamma_{ab}\Phi_j$, where Φ_j represents the usual autopower spectrum. We consider two different ways to parameterize Φ_j : (1) referred to as the ‘‘free spectrum’’ analysis, we model all Φ_j components independently and simultaneously; and (2) we assume a power-law spectral template across frequencies, in which case

$$\Phi_j = \frac{A^2}{12\pi^2 T} \left(\frac{f_j}{f_{\text{ref}}} \right)^{-\gamma} f_{\text{ref}}^{-3}, \quad (14)$$

where A is the characteristic strain at a reference frequency of $f_{\text{ref}} = 1 \text{ yr}^{-1}$, γ is the spectral index of the GWB’s power spectral density, and T is the total timing baseline of the data set. Approach (1) allows us to search for frequency-resolved anisotropy (i.e., we can measure anisotropy independently and simultaneously at all frequencies), while approach (2) searches for broadband anisotropy modeled on a GWB power-law spectrum. However, frequency-resolved anisotropy searches are computationally expensive given the large parameter space that must be explored, while searches that assume a power-law template for the GWB are more tractable.

The construction of the likelihood and priors and the sampling techniques are identical to those used in NG15gwb.

For the linear spherical-harmonic basis, we set uniform priors with boundaries $[-5, 5]$ on the spherical-harmonic coefficients, c_{lm} , and fix $c_{00} = \sqrt{4\pi}$ such that the variation in the monopole is modeled by the amplitude of the GWB. In this model, we do not impose a rejection prior on the sampled c_{lm} coefficients based on the physicality of the implied power distribution; this acts as a comparison for our other methods that do impose this restriction, and also enables this model to act more broadly as a diagnostic for potential systematics inducing deviations from the HD curve. For the square-root spherical-harmonic basis, we fix $b_{00} = 1$ to break scale and parity symmetries (Banagiri et al. 2021). Additionally, in this basis, the $\{b_{lm}\}$ parameters are complex-valued for $m \neq 0$, and we set the priors on the 2 degrees of freedom, the amplitude, $|b_{lm}|$, and phase, ϕ_{lm} , to be uniform between $[0, 50]$ and $[0, 2\pi]$, respectively. The b_{l0} parameters are real-valued (Banagiri et al. 2021), and we set uniform priors between $[-50, 50]$ for these parameters.

We measure the evidence for the presence of anisotropy by calculating the odds ratio between anisotropic and isotropic GWB models. Given the computational cost of the frequency-resolved anisotropy search, we measure the evidence for the presence of anisotropy in this analysis by calculating the Hellinger distance metric (Hellinger 1909) between the prior and posterior distributions of the angular power spectrum at each frequency. For two discrete probability distributions, $P = (p_1, \dots, p_k)$ and $Q = (q_1, \dots, q_k)$, the Hellinger distance is defined as (Hellinger 1909)

$$H(P, Q) = \frac{1}{\sqrt{2}} \sqrt{\sum_{i=1}^k (\sqrt{p_i} - \sqrt{q_i})^2}. \quad (15)$$

This is a bounded metric, $0 \leq H(P, Q) \leq 1$, such that a distance of 0 and 1 imply that P and Q are completely identical and distinct, respectively.

2.3. Frequentist Analysis Pipeline

The frequentist pipeline is based on using the pulsar cross-correlations as data, as described in Pol et al. (2022). The cross-correlations between two pulsars a and b , ρ_{ab} , and their uncertainties, σ_{ab} , are defined as (Demorest et al. 2013; Siemens et al. 2013; Chamberlin et al. 2015; Vigeland et al. 2018)

$$\begin{aligned} \rho_{ab} &= \frac{\delta \mathbf{t}_a^T \mathbf{N}_a^{-1} \hat{\mathbf{S}}_{ab} \mathbf{N}_b^{-1} \delta \mathbf{t}_b^T}{\text{tr}[\mathbf{N}_a^{-1} \hat{\mathbf{S}}_{ab} \mathbf{N}_b^{-1} \hat{\mathbf{S}}_{ba}]}, \\ \sigma_{ab} &= (\text{tr}[\mathbf{N}_a^{-1} \hat{\mathbf{S}}_{ab} \mathbf{N}_b^{-1} \hat{\mathbf{S}}_{ba}])^{-1/2}, \end{aligned} \quad (16)$$

where $\delta \mathbf{t}_a$ is a vector of timing residuals for pulsar a , $\mathbf{N}_a = \langle \delta \mathbf{t}_a \delta \mathbf{t}_a^T \rangle$ is the measured autocovariance matrix of pulsar a , and $\hat{\mathbf{S}}_{ab} \equiv \langle \delta \mathbf{t}_a \delta \mathbf{t}_b^T \rangle / \Gamma_{ab} A^2$ is the template-scaled covariance matrix between pulsars a and b . We use the formalism of Vigeland et al. (2018) to calculate the ‘‘noise-marginalized’’ optimal statistic (NMOS) cross-correlations and their uncertainties over multiple random draws from the posterior samples of a common uncorrelated red-noise Bayesian analysis (see NG15gwb for more details). This allows us to produce frequentist results that also marginalize over the intrinsic pulsar noise, similar to the Bayesian analyses.

PTA cross-correlation data can be modeled with the ORF from Equation (3), which can be further simplified into a general matrix form as $\Gamma = \mathbf{R}\mathbf{P}$, where Γ is an N_{cc} vector of

ORF values for all distinct pulsar pairs, \mathbf{P} is a vector describing the GWB power, and \mathbf{R} is a PTA overlap response matrix given by

$$R_{ab,k} = \frac{3}{2N_{\text{pix}}} [\mathcal{F}_{a,k}^+ \mathcal{F}_{b,k}^+ + \mathcal{F}_{a,k}^\times \mathcal{F}_{b,k}^\times], \quad (17)$$

where the normalization is chosen so that the ORF matches the HD values in the case of an isotropic GWB. We use the MAPS software package (Pol et al. 2022), which can model the GWB power in both the (normal and square-root) spherical-harmonic and pixel bases. As shown in Pol et al. (2022), the cross-correlation likelihood can be written as

$$p(\boldsymbol{\rho}|\mathbf{P}) = \frac{\exp\left[-\frac{1}{2}(\boldsymbol{\rho} - \mathbf{R}\mathbf{P})^T \boldsymbol{\Sigma}^{-1}(\boldsymbol{\rho} - \mathbf{R}\mathbf{P})\right]}{\sqrt{\det(2\pi\boldsymbol{\Sigma})}}, \quad (18)$$

where $\boldsymbol{\Sigma}$ is the diagonal covariance matrix of cross-correlation uncertainties, with shape $N_{\text{cc}} \times N_{\text{cc}}$.

For the radiometer pixel and (linear) spherical-harmonic basis, the problem is linear in the regression coefficients (i.e., pixel amplitude and spherical-harmonic coefficients). So the maximum likelihood solution can be derived analytically (Thrane et al. 2009; Romano & Cornish 2017; Ivezić et al. 2019):

$$\hat{\mathbf{P}} = \mathbf{M}^{-1}\mathbf{X}, \quad (19)$$

where $\mathbf{M} = \mathbf{R}^T \boldsymbol{\Sigma}^{-1} \mathbf{R}$ is the Fisher information matrix, with uncertainties on the regression parameters given by the diagonal elements of \mathbf{M}^{-1} , and $\mathbf{X} = \mathbf{R}^T \boldsymbol{\Sigma}^{-1} \boldsymbol{\rho}$ is the “dirty map,” an inverse-noise-weighted representation of the total power on the sky as seen through the response of the pulsars in the PTA. Note that for the radiometer pixel basis, since the individual pixels are modeled independently, the inverse of the full Fisher matrix in Equation (19) is replaced by the inverse of the diagonal elements of the Fisher matrix to obtain an estimate of the amplitude in any given pixel (Romano & Cornish 2017). For the square-root spherical-harmonic basis, since the problem is nonlinear in the regression coefficients (i.e., the b_{lm} parameters), the maximum likelihood solution is derived using numerical optimization techniques. As described in Pol et al. (2022), we use the LMFIT (Newville et al. 2021) Python package with Levenberg–Marquardt optimization (Levenberg 1944; Marquardt 1963) to calculate the maximum likelihood solution.

For the spherical-harmonic basis, we define three types of signal-to-noise ratios (S/Ns) through the maximum likelihood ratio (Pol et al. 2022): (i) the total S/N, defined as the maximum likelihood ratio between an anisotropic model and noise; (ii) isotropic S/N, defined as the maximum likelihood ratio between an isotropic model and noise; and (iii) anisotropic S/N, defined as the maximum likelihood ratio between an anisotropic model and an isotropic model. Together, these S/Ns provide a complete description of the correlations that might be present in the data. To interpret the S/N values, we calibrate them against a null distribution that is constructed using the measured uncertainties for the pairwise cross-correlations. Since the null hypothesis when searching for anisotropy is isotropy, we construct the null hypothesis by generating draws for each pulsar pair from a Gaussian distribution whose mean is the theoretical HD value and standard deviation is the cross-

correlation uncertainty measured from the real data set. For each of these “realizations” of the null distribution, we calculate the S/Ns and calibrate the significance of the S/N values measured with the real data set through p -values, where a p -value $p < 3 \times 10^{-3}$ (corresponding to a 3σ Gaussian-equivalent threshold) would imply a significant detection of anisotropy. We also use these null distributions to define the “decision threshold,” C_l^{th} , for each spherical-harmonic multipole, such that if the measured angular power at any multipole is above this decision threshold, that would imply the measured angular power is inconsistent with the null hypothesis at the 3σ level (Pol et al. 2022). The decision threshold allows us to search for the presence of anisotropy at a single multipole, while the S/Ns represent holistic evidence for the presence of anisotropy in the data.

For the radiometer pixel basis, we define our detection statistic as the ratio of the power, $P_{\hat{\Omega}}$, measured in each pixel to the uncertainty, $\sigma_{P_{\hat{\Omega}}}$, on that measurement, i.e., $P_{\hat{\Omega}}/\sigma_{P_{\hat{\Omega}}}$. For each of the realizations of the null hypothesis described above, we calculate the corresponding sky maps and uncertainties, compute the detection statistic for each pixel, and construct the null distribution for each individual pixel across realizations of the null hypothesis. We use this null distribution per pixel in conjunction with dividing our p -value threshold of 3×10^{-3} ($\sim 3\sigma$) by a trials factor, $n = N_{\text{pix}}$, to calibrate the significance of the detection statistic measured in the real data.

3. Results

In *NG15gwb*, the low-frequency GWB signal is described using the lowest 14 frequency bins when using the full set of correlations. However, most of the support for HD correlations in the data is concentrated in the lowest five frequency bins, with the higher-frequency bins showing evidence for the autocorrelations. As a result, we use the lowest five frequency bins to model the anisotropy in the GWB, but perform a few analyses using 14 frequency bins and find no significant difference from our results using the lowest five bins.

In the Bayesian analysis, we model the GWB as a power law with both a fixed $\gamma = 13/3$ (Phinney 2001) and varied spectral index. We also model the anisotropy at each of the lowest five Fourier frequency bins simultaneously, as different SMBHB systems will contribute to different frequency bins resulting in unique anisotropy signatures at different frequencies, which might not be detectable under a power-law template for the GWB. The spectral template of the GWB in the frequentist analyses is limited to a power-law template, again using just the lowest five frequency bins. Given the results from *NG15gwb*, we search for anisotropy at spectral indices of $\gamma = 3.2$, corresponding to the maximum a posteriori value, and $\gamma = 13/3$.

As described in Sections 2.1.1 and 2.1.2, the diffraction limit defines an optimal choice of $N_{\text{side}} = 8$ and $l_{\text{max}} = 8$ for the pixel and spherical-harmonic bases, respectively. Floden et al. (2022) showed that searches at multipoles higher than l_{max} can be feasible, though this results in a reduction in the overall S/N of any anisotropic signal that might be present in the data. To test whether the choice of l_{max} defined by the diffraction limit is supported by the data, we calculate the maximum likelihood S/N values as a function of l_{max} . As shown in Figure 1, we see that the total and anisotropic S/Ns start to saturate at $l_{\text{max}} = 6$, slightly lower than the diffraction limit implied $l_{\text{max}} = 8$. To

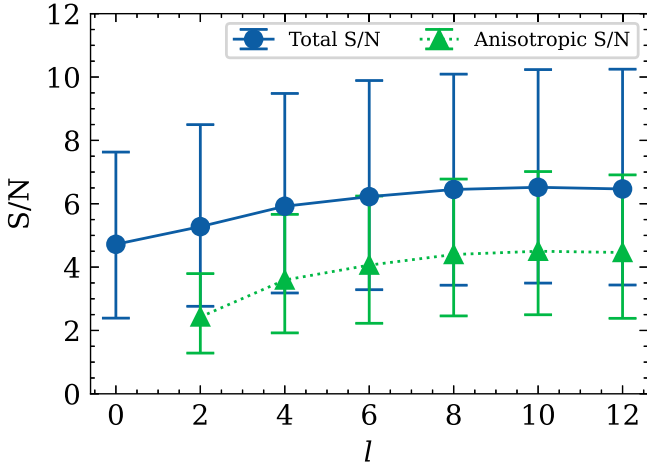


Figure 1. The total and anisotropic signal-to-noise ratio (S/N) derived using the frequentist square-root spherical-harmonic basis described in Section 2.3. Both the total and anisotropic S/Ns start to saturate at an $l_{\max} = 6$, which we choose for all the analyses presented in this work.

prevent overfitting the data, we set $l_{\max} = 6$ for all of our analyses.

3.1. Detector Antenna Response

The directional response of any single pulsar, a , in the PTA to the presence of a (anisotropic) GWB is quantified through the antenna response pattern in Equation (2), while the response of the correlations between a pair of pulsars, a, b , is quantified by the term in the parentheses in Equations (1) and (3) (Romano & Cornish 2017). However, given that no two pulsars in the PTA are identical, it is important to weigh the response of each pulsar pair by the corresponding uncertainty on the measured cross-correlations between that pair of pulsars. The directional sensitivity of the PTA can thus be gauged through the diagonal elements of the Fisher matrix, \mathbf{M} , introduced in Section 2.3. Figure 2 shows the median of $\sqrt{\mathcal{M}(\hat{\Omega})}$, the normalized square root of the diagonal elements of the Fisher matrix, across 5000 draws from the NMOS. Since $\sqrt{\mathbf{M}^{-1}}$ represents the uncertainty on the amplitude measured in each pixel in the radiometer pixel basis, this map represents the relative sensitivity of the NANOGrav 15 yr data set to different directions on the sky. As we can see, the detector has the highest sensitivity where it has the highest density of pulsars. Note that the cross-correlation uncertainties used in calculating this map are derived from using a power-law template for the GWB, and the detector antenna response may be slightly different at different frequencies.

3.2. Spherical-harmonic Basis

We show the distribution of the measured anisotropic S/N measured from 5000 draws from the NMOS in Figure 3, along with the distribution for the S/N under the null hypothesis of an isotropic GWB. We measure an anisotropic S/N of ≈ 4 , which corresponds to a significance at the $p = 0.05$ level. Thus, while there is some evidence for the presence of anisotropy in the 15 yr data set, it does not yet rise to the level of a “significant” detection, i.e., $p > 3 \times 10^{-3}$ (Section 2.3). We also measure the angular power at each multipole, as shown in Figure 4 along with the decision threshold (see Section 2.3). As the power in any of the multipoles does not rise above the

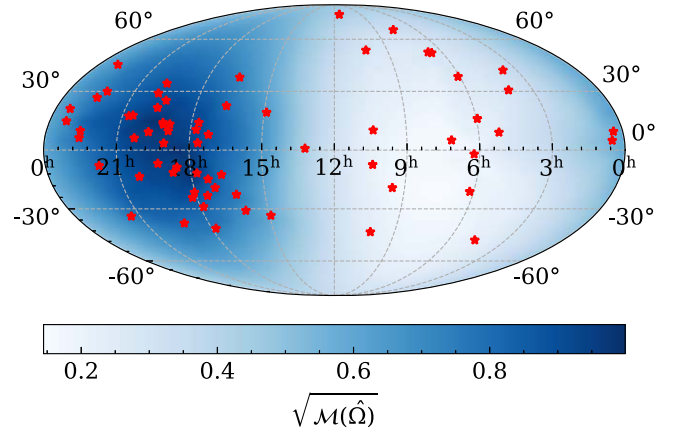


Figure 2. The normalized square root of the diagonal elements of the Fisher matrix over 5000 draws from the NMOS cross-correlation uncertainties, representing the relative sensitivity of the PTA to anisotropy in different directions on the sky. As expected, the PTA has the highest sensitivity in the part of the sky that has the highest density of pulsars.

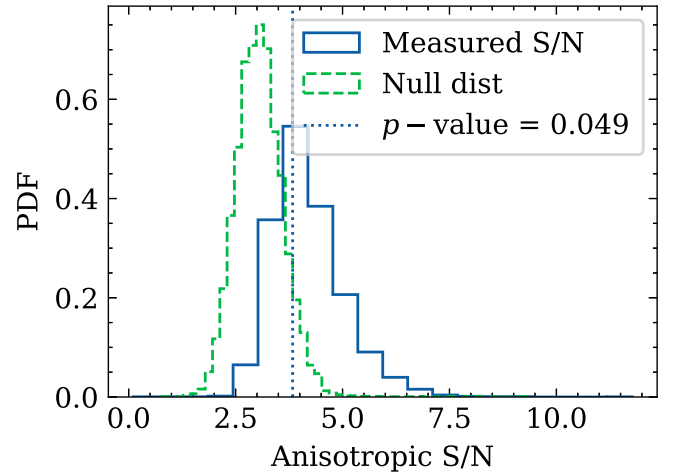


Figure 3. The noise-marginalized distribution of the anisotropic S/N is shown along with the anisotropic S/N derived under the null hypothesis of an isotropic GWB (Section 2.3). The mode of the measured anisotropic S/N corresponds to a p -value of $p = 0.05$, which is greater than our $p < 3 \times 10^{-3}$ threshold (Section 2.3), implying that we do not have a significant detection of anisotropy in this data set.

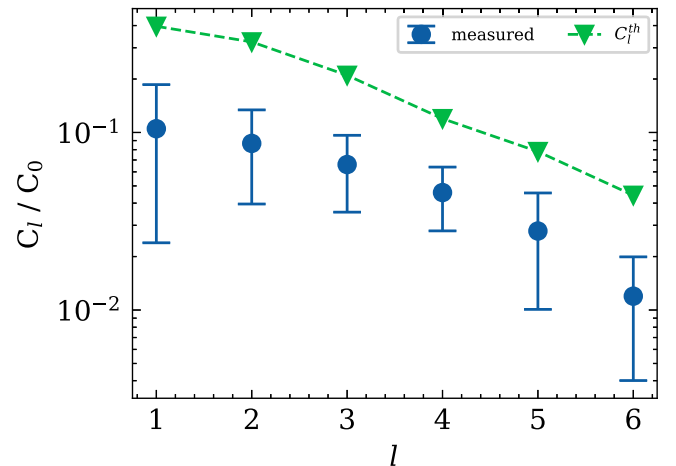


Figure 4. The angular power spectrum and decision threshold (Section 2.3) measured using the frequentist square-root spherical-harmonic basis. The measured power does not rise above the decision threshold for any multipole, implying that the data are consistent with isotropic GWB.

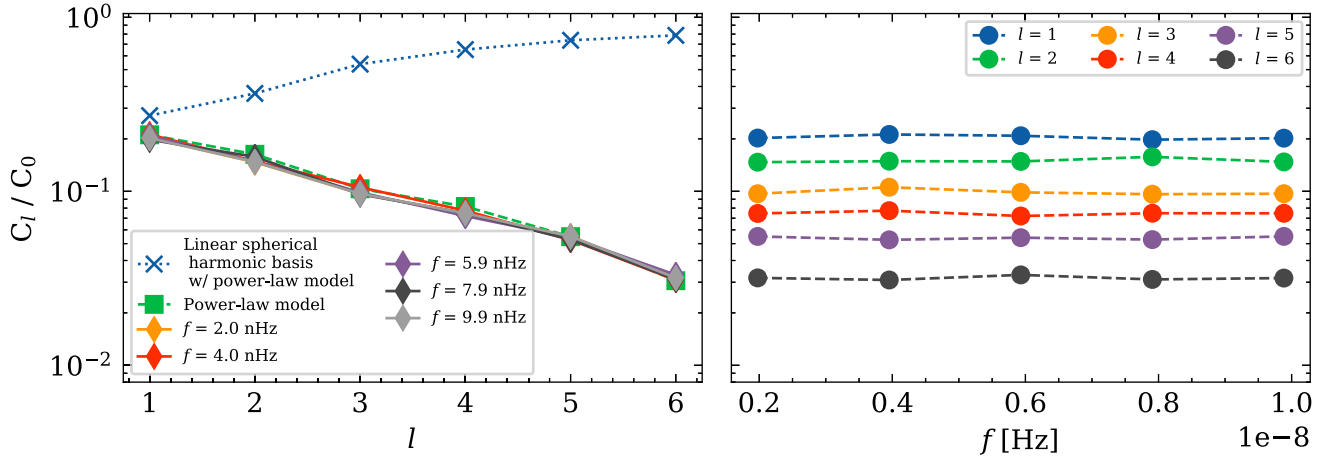


Figure 5. Left: the 95% upper limits on the angular power spectrum derived from the Bayesian linear (dotted line with cross marker) and square-root (dashed line with square marker) spherical-harmonic basis using a lowest-five-frequency-bin power-law template for the anisotropic GWB while varying the spectral index. For the latter, we also show the 95% upper limits on the angular spectrum when searching for anisotropy in the lowest five bins simultaneously. For the square-root spherical-harmonic basis, the evolution of the upper limits as a function of spherical-harmonic multipoles reflects the constraint from the prior condition that the power be positive on the sky as imposed by the square-root spherical-harmonic basis. The similarity of the upper limits on the dipole between the linear and square-root spherical-harmonic basis implies that the dipole may be close to the data-informed regime. Right: the 95% upper limits at different spherical-harmonic multipoles as a function of frequency for the square-root spherical-harmonic basis. The lack of frequency dependence in the upper limits implies that the sensitivity to anisotropy at each frequency is defined by the sensitivity of the overall PTA to the GWB at each of those frequencies.

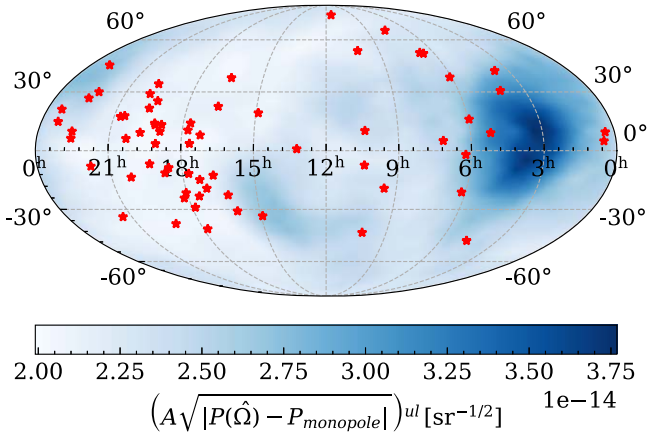


Figure 6. Reconstructed sky map from the Bayesian square-root spherical-harmonic basis showing the 95% upper limit on deviations away from the isotropic component of the GWB, where the red stars represent the position of pulsars in the PTA. The power is represented in terms of the characteristic strain, referenced to a frequency of $f_{\text{ref}} = 1 \text{ yr}^{-1} \text{ sr}^{-1/2}$, marginalizing over the spectral index of the GWB. The odds ratio in favor of anisotropy over isotropy for the GWB ≈ 2 , implying no significant detection of anisotropy in this data set.

decision threshold, the data are consistent with isotropy at all spherical-harmonic multipoles.

The search for anisotropy using our Bayesian pipeline produces results that are consistent with the frequentist results described above. We find an odds ratio of ≈ 2 in favor of an anisotropic model for the GWB using the square-root spherical-harmonic basis, consistent with the nondetection in the frequentist analysis. Given the lack of detection, we plot the 95% credible upper limit on the angular power spectrum calculated using both the linear and square-root spherical-harmonic bases in Figure 5 and show the reconstructed 95% upper limits on deviations away from isotropy in Figure 6. We also search for anisotropy simultaneously in each of the lowest five frequency bins of the detector and find that our analysis returns the priors, as shown using the Hellinger distance metric

in Figure 7 implying no significant detection of anisotropy. Consequently, we show the 95% upper limits for the angular power spectrum at each of these frequencies in Figure 5 and the reconstructed 95% upper limits on deviations away from isotropy for these five frequencies in Figure 8.

3.3. Radiometer Pixel Basis

Figure 9 shows the median of the noise-marginalized radiometer pixel map, along with the p -values corresponding to each pixel, calculated as described in Section 2.3, and shows that we do not detect significant power in any single pixel. Note that the frequentist analysis for this basis does not impose the condition that the power be positive across all sky, resulting in negative power in some parts of the sky.

We also show the results from a Bayesian radiometer pixel analysis in Figure 10, where we plot the median power in each pixel. Since the GWB strain amplitude priors in the Bayesian analysis are log-uniform between 10^{-18} – 10^{-14} , we intrinsically restrict the power to be positive across all sky. Even though we observe some pixels with $A(\hat{\Omega}) \geq 5 \times 10^{-15}$, the odds ratios imply the data prefer an isotropic all-sky GWB over GWs originating from these pixels.

4. Discussion

In this analysis, we search for anisotropy in the NANOGrav 15 yr data set using the full set of correlation information. We do not find significant evidence for the presence of either power-law or frequency-resolved anisotropy.

However, we observe features in the reconstructed sky maps that could be an early indication of anisotropy in the GWB. As shown in Figure 6, we recover larger limits on deviations from isotropy at $\text{RA} \approx 3^{\text{h}}$ than elsewhere in the maps derived using the Bayesian square-root spherical-harmonic analyses. In the frequency-resolved Bayesian anisotropy analysis, this same approximate feature appears in all of the lowest five frequency bins. This is likely indicative of the power-law template

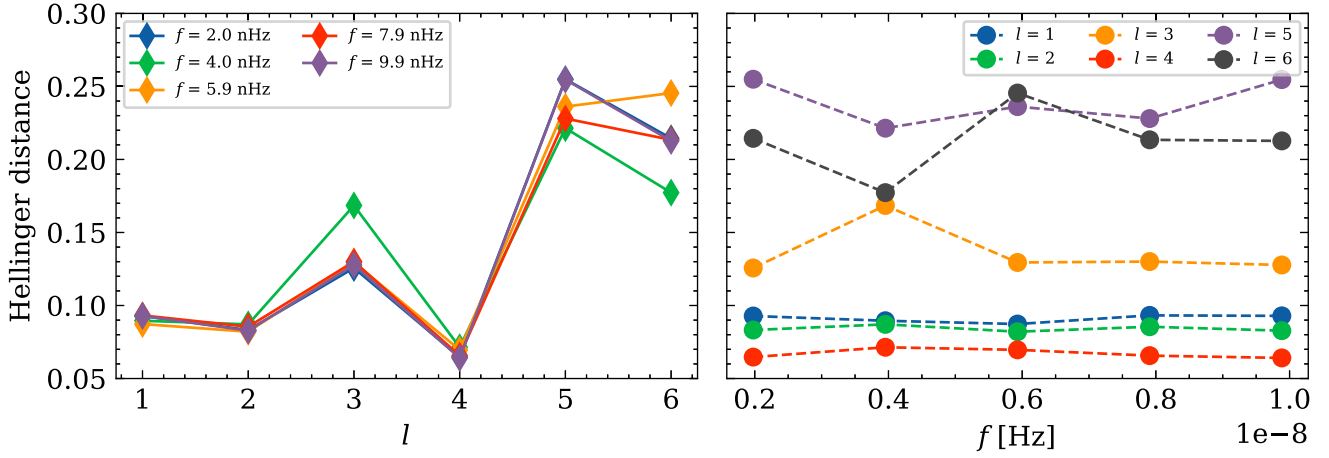


Figure 7. The Hellinger distance between posterior and prior distributions of C_l/C_0 for the frequency-resolved anisotropy analysis. A Hellinger distance of 0 and 1 imply that the two distributions are identical and distinct respectively. Left: the Hellinger distance for different frequencies as a function of spherical-harmonic multipoles. Right: the Hellinger distance for different spherical-harmonic multipoles as a function of frequency. This plot shows that there is no significant difference between the posterior and prior distributions of the angular power for any of the lowest five frequencies, implying that the data are consistent with isotropy in these bins.

(restricted to the lowest five frequency bins) producing a representation of anisotropy that is averaged across the frequency bins used in the analysis. There is also excess power in this location in both the frequentist and Bayesian radiometer pixel analyses; it will be interesting to monitor these features in future data sets. We also note that the upper limits derived here on the anisotropy in different directions on the sky are higher than the limits set in a directed search for GWs from individual SMBHB systems (Arzoumanian et al. 2023).

We also show that there is no significant evidence (Figure 7) for anisotropy in the second frequency bin, where NG15gwb reported excess power with “monopolar”⁶⁷ correlations. The reconstructed sky map (top right panel of Figure 8) also does not show features that are significantly different from the maps produced for other frequency bins. Thus, we are unable to confirm if the “monopolar” correlation signature observed in NG15gwb is due to the presence of anisotropy in this frequency bin. While analytic (Mingarelli et al. 2013; Hotinli et al. 2019; Sato-Polito & Kamionkowski 2023), semianalytic (Mingarelli et al. 2017), and simulation-based (Taylor & Gair 2013; Taylor et al. 2020) estimates for SMBHB-produced anisotropy have been proposed, they are all dependent on different model choices for the populations. However, we can use the GWB parameters measured in NG15gwb to make estimates of the expected level of anisotropy for SMBHB systems that are distributed randomly on the sky. The random distribution of SMBHB systems on the sky implicitly assumes that the large-scale structure is isotropic at these distances, implying that the estimates on anisotropy produced here will be pessimistic in nature. However, these estimates can serve as targets for PTAs to achieve in forthcoming data sets, by growing the array and increasing timing precision.

To calculate the estimates conditioned on the GWB parameters in NG15gwb, we use SMBHB populations generated with holodeck (Agazie et al. 2023d), following semianalytic prescriptions for galaxy stellar mass function (GSMF), galaxy pair fraction, galaxy merger time, and black

hole–bulge mass relations. These populations are then evolved in time using a self-consistent binary evolution model to produce an expectation value for the number of binaries of each SMBHB parameter (see Agazie et al. 2023d for details). We generate individual universe realizations by drawing randomly from a Poisson distribution around this expectation value. To model the anisotropy of populations consistent with current GWB measurements, we select the 100 samples that best match the 15 yr characteristic strain amplitude measurement of $h_c = 11.2 \times 10^{-15}$ at $f = 0.1 \text{ yr}^{-1}$ (Agazie et al. 2023b) from a set of 1000 samples of varying GSMF, black hole–bulge mass relation, and hardening time parameters.

Because the loudest single sources determine the level of anisotropy (Bécsy et al. 2022), one can treat all but the 2000 loudest as perfectly isotropic. Thus, for each realization, we select the 2000 loudest single sources in each frequency bin, place these single sources randomly on a HEALpix map of the sky with $N_{\text{side}} = 32$ (Górski et al. 2005), and divide the characteristic strain of the background (all other sources) evenly among all pixels on the map. Finally, we calculate the spherical harmonics of these maps using the HEALPix anafast program with $l_{\text{max}} = 6$ to maintain consistency with the detection analysis presented in this work.

The normalized spherical-harmonic coefficients C_l/C_0 of these samples are shown in Figure 11 with solid lines representing the median over samples and shaded regions being the 68% confidence intervals. These samples’ 68% confidence interval spans approximately 1 order of magnitude for all harmonics, but demonstrates a general power-law-like increase in anisotropy with increasing frequency, their medians going from $C_l/C_0 \sim 4 \times 10^{-2}$ at $f = 0.10 \text{ yr}^{-1}$ to $C_l/C_0 \sim 2 \times 10^{-1}$ at $f = 1.0 \text{ yr}^{-1}$. The results are indistinguishable between different harmonics of $l > 0$, consistent with the analytic model analogous to large-scale structure shot noise in Sato-Polito & Kamionkowski (2023).

For comparison, the Bayesian upper limits for spherical harmonics $l = 1$ to $l = 6$ from Figure 5 are plotted alongside the simulated SMBHB anisotropy in Figure 11 as circles connected by dashed lines. Each upper limit falls within the 68% confidence interval region for most frequencies, and the $l = 2$ to $l = 5$ upper limits also intersect the median predictions. Unlike

⁶⁷ Note that monopolar correlations here refer to a correlation signature described by a constant offset as in NG15gwb and not the “monopole” as referred to in the spherical-harmonic basis where it represents the isotropic component of the signal.

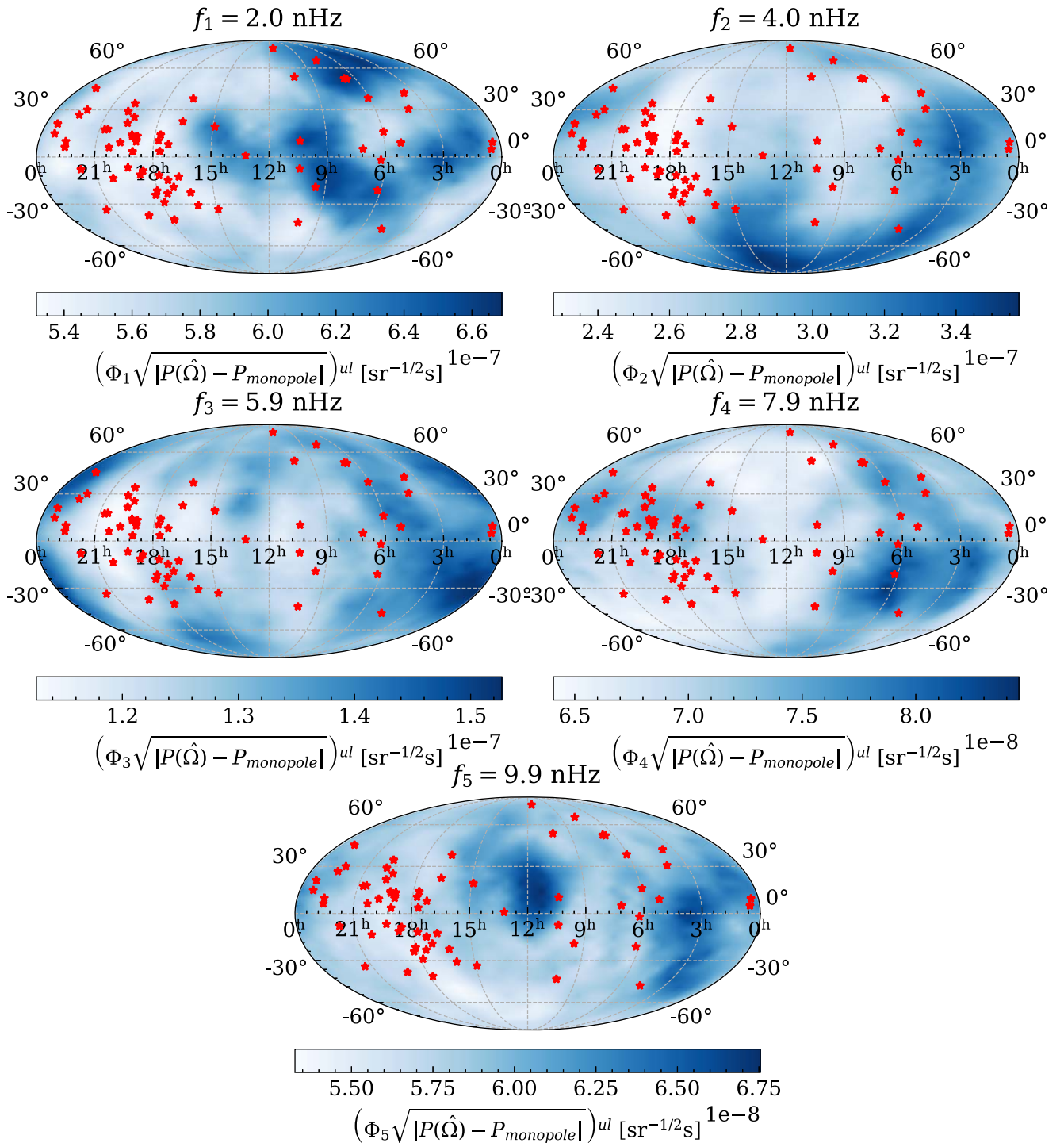


Figure 8. Reconstructed frequency-resolved sky maps from the Bayesian square-root spherical-harmonic basis showing the 95% upper limit on the deviation away from the isotropic component of the GWB. The red stars represent the position of the pulsars in the PTA. The units for the power in these maps are $\text{sr}^{-1/2}$ and represent the excess timing delay, adopted for ease of comparison to Figure 1(a) in [NG15gwb](#).

the simulated estimates of anisotropy that increase with frequency but are the same for all l , the upper limits are uniform across frequencies but decrease with l by about 1 order of magnitude from $l = 1$ to $l = 6$. As such, we find these upper limits fall just below the 68% confidence intervals for the lowest (nonzero) harmonics at low frequencies (2 nHz) and just below the simulated C_l/C_0 68% confidence intervals for high harmonic ($l = 6$) at high frequencies (10 nHz). Thus, PTAs are likely to first detect small-scale anisotropy (larger values of l)

before they detect large-scale anisotropy (smaller values of l) using the spherical-harmonic basis.

5. Conclusion and Future prospects

We search for anisotropy in the NANOGrav 15 yr data set and do not find significant evidence in favor of its presence in the GWB. As PTA data sets grow in time and add more pulsars to the array, the sensitivity of the detector to anisotropy in the GWB will increase (Taylor et al. 2020; Pol et al. 2022) and

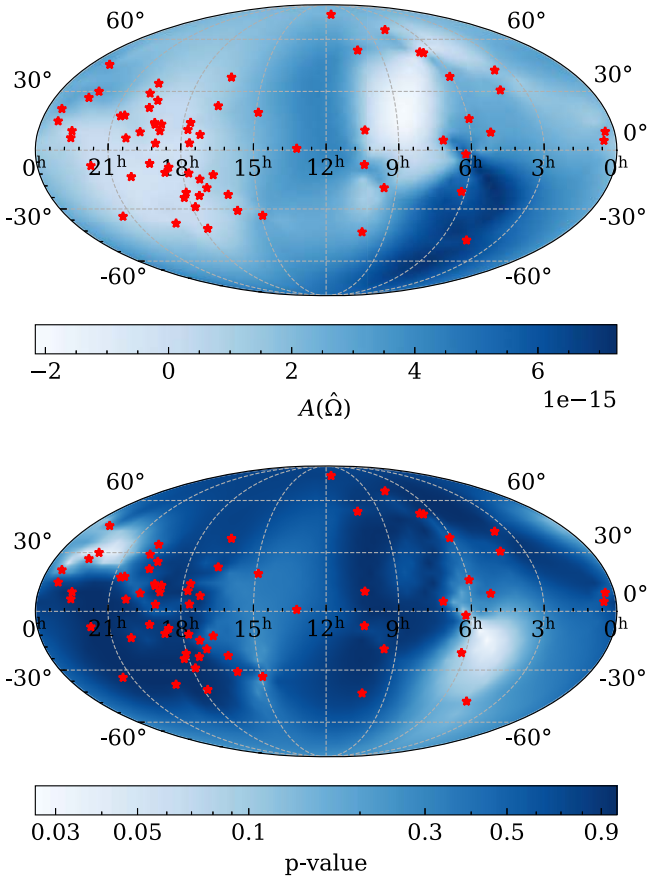


Figure 9. Top: power measured at each pixel using the frequentist radiometer pixel basis, in units of characteristic strain. This map was constructed with $N_{\text{side}} = 8$, resulting in 768 pixels on the sky. The negative recovered power is a consequence of this analysis not imposing the condition that the power be positive across all sky. Bottom: the p -value corresponding to the detection statistic for each pixel shown in the top panel. All of the measured p -values imply that the data are consistent with isotropy.

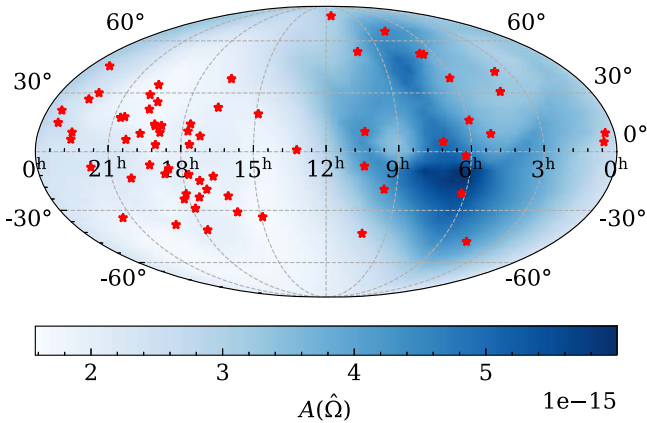


Figure 10. Power measured at each pixel using the Bayesian radiometer pixel basis, in units of characteristic strain, with the red stars showing the position of pulsars in the PTA. This map was constructed with $N_{\text{side}} = 8$, resulting in 768 pixels on the sky. Since the prior on the GWB amplitude was log-uniform between 10^{-18} and 10^{-14} , the power was also constrained to be positive across the sky. The sky map is qualitatively consistent with the map derived using the frequentist radiometer pixel basis analysis.

allow us to conclusively determine if the features observed in the reconstructed GWB sky maps in this data set are real. The International Pulsar Timing Array’s (IPTA; Hobbs et al. 2010;

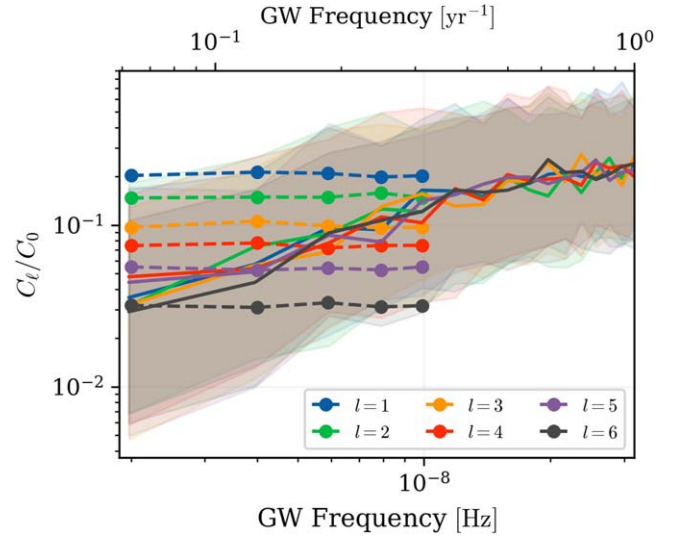


Figure 11. Normalized spherical-harmonic coefficients C_l/C_0 of the gravitational-wave sky as produced by simulated populations of SMBHBs, filtered by consistency with the 15 yr isotropic gravitational-wave background estimation (Agazie et al. 2023b). The different colors correspond to individual harmonics from $l = 1$ to $l = 6$. The solid lines represent the median realization of the median samples, and the shaded regions represent the 68% confidence intervals across all samples’ median realizations. The circles connected by dashed lines represent the Bayesian upper limits as in Figure 5.

Perera et al. 2019) third data release (DR3), currently under preparation, will combine the NANOGrav 15 yr data set with the latest data sets from the European (Kramer & Champion 2013), Indian (Joshi et al. 2018), South African (MeerTIME; Bailes et al. 2020), and Parkes (Hobbs 2013) PTAs. This combined data set is projected to have approximately 100 pulsars (an increase of $\approx 20\%$ over the NANOGrav 15 yr data set) and a maximum baseline of 24 yr (an increase of $\approx 60\%$ over the NANOGrav 15 yr data set), and should consequently have better sensitivity to any anisotropy that might be present in the GWB.

As we head into this new era in nanohertz GW astronomy with PTA data sets growing their timing baselines and quantity of pulsars, new methods will need to be developed in order to efficiently search for anisotropy in these PTA data sets. The frequentist analyses implemented in this work are computationally efficient and have a small turnaround time for producing end-to-end results. However, the current implementation of the optimal statistic does not account for inter-pulsar-pair covariance (Romano et al. 2021; Allen & Romano 2023) and cosmic variance (Allen 2023), and does not include information contained in the autocorrelations of the pulsar data set. While the Bayesian analyses do not suffer from some of these drawbacks, they are computationally expensive and can take weeks for the Markov Chain Monte Carlo (MCMC) chains to burn-in and converge for the power-law anisotropy models, and even longer when searching for frequency-resolved anisotropy. It also takes a significant amount of time to scan across an $N_{\text{side}} = 8$ sky in the Bayesian radiometer pixel analyses, and this time will increase with increasing values of N_{side} .

One possible solution, currently under development, would be to formulate a method that can leverage Fourier basis coefficients used to model the GWB in the Bayesian analysis to directly calculate both the auto- and cross-correlations between the pulsars in the array. The frequentist framework developed

in Pol et al. (2022) and used in this work is agnostic to the method used to calculate the correlations and can be adapted to include the autocorrelation information. Another solution would be to implement more sophisticated MCMC sampling techniques, such as reversible-jump MCMC (RJCMC), which has already been implemented for single-source searches (Bécsy & Cornish 2020), and apply them to searches for anisotropy. RJCMC, in particular, has the potential to significantly boost the efficiency of the Bayesian frequency-resolved and radiometer pixel searches since it has the capability to simultaneously search over multiple models (in this case frequencies or pixels, respectively) as well as to calculate the odds ratios between these models. Additionally, future mock data challenges like those carried out by the IPTA (Ellis et al. 2012; Hazboun et al. 2018) will be crucial in developing new methods as well as testing the efficacy of current methods to detect anisotropy in realistic PTA data sets.

As the evidence for an isotropic GWB continues to grow with future data sets (Pol et al. 2021), it will become more prudent to search for the presence of anisotropy in the GWB. Since cosmological sources of a nanohertz GWB like cosmic strings are unlikely to produce an anisotropic GWB (Ölmez et al. 2012), detection of anisotropy will be an important piece of evidence in support of SMBHBs as the origin of the nanohertz GWB. A detection of pixel-scale anisotropy could provide the first indication of a single inspiraling SMBHB system that could then be subjected to targeted follow-up using both PTA GW and electromagnetic observatories. A detection of large-scale anisotropy could indicate an overdensity of SMBHB systems in a cluster environment, or might point to an extrinsic effect (Chung et al. 2022), such as the kinematic dipole observed with the cosmic microwave background (Planck Collaboration et al. 2020) and predicted to be detectable with a GWB (Bertacca et al. 2020; Chung et al. 2022; Cusin & Tasinato 2022; Valbusa Dall’Armi et al. 2022). If we live in a Universe where both astrophysical (e.g., from SMBHBs) and cosmological (e.g., from cosmic strings) GWBs are present, we can leverage our knowledge of the different expected spatial (and spectral) distribution of these processes to disentangle them in the PTA data sets (Ungarelli & Vecchio 2001; Mandic et al. 2012; Parida et al. 2016; Biscoveanu et al. 2020; Martinovic et al. 2021; Suresh et al. 2021; Kaiser et al. 2022). It will also be prudent to search for and possibly rule out anisotropy in the GWB before other interpretations of deviations away from the theoretical HD curve, such as beyond-GR effects (e.g., Arzoumanian et al. 2021), are accepted. Thus, detection of anisotropy in the GWB is poised to be one of the next milestones in nanohertz GW astronomy, potentially leading us toward the detection of one or more isolated GW sources and allowing us to place constraints on beyond Standard Model physics.

Acknowledgments

Author contributions. An alphabetical-order author list was used for this Letter in recognition of the fact that a large, decade-timescale project such as NANOGrav is necessarily the result of the work of many people. All authors contributed to the activities of the NANOGrav collaboration leading to the work presented here, and reviewed the manuscript, text, and figures prior to the Letter’s submission. Additional specific contributions to this Letter are as follows. N.S.P., S.R.T., and J.D.R. proposed and planned this analysis. N.S.P. coordinated

the execution of the analysis and writing of this Letter. N.S.P., S.R.T., E.C.G., L.Z.K., J.D.R., K.D.O., P.M., and N.L. contributed text to the Letter. N.S.P. led the frequentist analyses, N.L. and L.S. led the Bayesian analyses, and E.C.G. led the HOLODECK-based astrophysical simulation analyses, all of which had input from S.R.T., J.D.R., L.Z.K., K.O., and P.M. The NANOGrav 15 yr data set was developed by G.A., A.A., A.M.A., Z.A., P.T.B., P.R.B., H.T.C., K.C., M.E.D., P.B.D., T.D., E.C.F., W.F., E.F., G.E.F., N.G., P.A.G., J.G., D.C.G., J.S.H., R.J.J., M.L.J., D.L.K., M.K., M.T.L., D.R.L., J.L., R.S.L., A.M., M.A.M., N.M., B.W.M., C.N., D.J.N., T.T.P., B.B.P.P., N.S.P., H.A.R., S.M.R., P.S.R., A.S., C.S., B.J.S., I.H.S., K.S., A.S., J.K.S., and H.M.W. through a combination of observations, arrival time calculations, data checks and refinements, and timing model development and analysis; additional specific contributions to the data set are summarized in [NG15dataset](#).

The NANOGrav collaboration receives support from National Science Foundation (NSF) Physics Frontiers Center award numbers 1430284 and 2020265, the Gordon and Betty Moore Foundation, NSF AccelNet award number 2114721, an NSERC Discovery Grant, and CIFAR. The Arecibo Observatory is a facility of the NSF operated under cooperative agreement (AST-1744119) by the University of Central Florida (UCF) in alliance with Universidad Ana G. Méndez (UAGM) and Yang Enterprises (YEI), Inc. The Green Bank Observatory is a facility of the NSF operated under cooperative agreement by Associated Universities, Inc. The National Radio Astronomy Observatory is a facility of the NSF operated under cooperative agreement by Associated Universities, Inc. This work was conducted in part using the resources of the Advanced Computing Center for Research and Education (ACCRE) at Vanderbilt University, Nashville, TN.

L.B. acknowledges support from the National Science Foundation under award AST-1909933 and from the Research Corporation for Science Advancement under Cottrell Scholar Award No. 27553. P.R.B. is supported by the Science and Technology Facilities Council, grant number ST/W000946/1. S.B. gratefully acknowledges the support of a Sloan Fellowship, and the support of NSF under award #1815664. M.C. and S.R.T. acknowledge support from NSF AST-2007993. M.C. and N.S.P. were supported by the Vanderbilt Initiative in Data Intensive Astrophysics (VIDA) Fellowship. Support for this work was provided by the NSF through the Grote Reber Fellowship Program administered by Associated Universities, Inc./National Radio Astronomy Observatory. Support for H.T.C. is provided by NASA through the NASA Hubble Fellowship Program grant #HST-HF2-51453.001 awarded by the Space Telescope Science Institute, which is operated by the Association of Universities for Research in Astronomy, Inc., for NASA, under contract NAS5-26555. Pulsar research at UBC is supported by an NSERC Discovery Grant and by CIFAR. K.C. is supported by a UBC Four Year Fellowship (6456). M.E.D. acknowledges support from the Naval Research Laboratory by NASA under contract S-15633Y. T.D. and M.T.L. are supported by an NSF Astronomy and Astrophysics Grant (AAG) award number 2009468. E.C.F. is supported by NASA under award number 80GSFC21M0002. G.E.F., S.C.S., and S.J.V. are supported by NSF award PHY-2011772. The Flatiron Institute is supported by the Simons Foundation. A.D.J. and M.V. acknowledge support from the Caltech and Jet Propulsion Laboratory President’s and

Director’s Research and Development Fund. A.D.J. acknowledges support from the Sloan Foundation. The work of N.La. and X.S. is partly supported by the George and Hannah Bolinger Memorial Fund in the College of Science at Oregon State University. N.La. acknowledges the support from Larry W. Martin and Joyce B. O’Neill Endowed Fellowship in the College of Science at Oregon State University. Part of this research was carried out at the Jet Propulsion Laboratory, California Institute of Technology, under a contract with the National Aeronautics and Space Administration (80NM0018D0004). D.R.L. and M.A.M. are supported by NSF #1458952. M.A.M. is supported by NSF #2009425. C. M.F.M. was supported in part by the National Science Foundation under grant Nos. NSF PHY-1748958 and AST-2106552. A.Mi. is supported by the Deutsche Forschungsgemeinschaft under Germany’s Excellence Strategy—EXC 2121 Quantum Universe—390833306. The Dunlap Institute is funded by an endowment established by the David Dunlap family and the University of Toronto. K.D.O. was supported in part by NSF grant No. 2207267. T.T.P. acknowledges support from the Extragalactic Astrophysics Research Group at Eötvös Loránd University, funded by the Eötvös Loránd Research Network (ELKH), which was used during the development of this research. S.M.R. and I.H.S. are CIFAR Fellows. Portions of this work performed at NRL were supported by ONR 6.1 basic research funding. J.D.R. also acknowledges support from start-up funds from Texas Tech University. J.S. is supported by an NSF Astronomy and Astrophysics Postdoctoral Fellowship under award AST-2202388, and acknowledges previous support by the NSF under award 1847938. S.R.T. acknowledges support from an NSF CAREER award #2146016. C.U. acknowledges support from BGU (Kreitman fellowship), and the Council for Higher Education and Israel Academy of Sciences and Humanities (Excellence fellowship). C.A.W. acknowledges support from CIERA, the Adler Planetarium, and the Brinson Foundation through a CIERA-Adler postdoctoral fellowship. O.Y. is supported by the National Science Foundation Graduate Research Fellowship under grant No. DGE-2139292.

Facilities: Arecibo, GBT, VLA.

Software: `astropy` (Astropy Collaboration et al. 2022), `ENTERPRISE` (Ellis et al. 2020), `enterprise_extensions` (Taylor et al. 2021), `healpy` (Zonca et al. 2019), `holodeck` (Agazie et al. 2023d), `Jupyter` (Kluyver et al. 2016), `MAPS` (Pol et al. 2022), `matplotlib` (Hunter 2007), `numpy` (Harris et al. 2020), `PTMCMC` (Ellis & van Haasteren 2017), `scipy` (Virtanen et al. 2020).

ORCID iDs

Gabriella Agazie <https://orcid.org/0000-0001-5134-3925>

Akash Anumarlapudi <https://orcid.org/0000-0002-8935-9882>

Anne M. Archibald <https://orcid.org/0000-0003-0638-3340>

Paul T. Baker <https://orcid.org/0000-0003-2745-753X>

Bence Bécsy <https://orcid.org/0000-0003-0909-5563>

Laura Blecha <https://orcid.org/0000-0002-2183-1087>

Adam Brazier <https://orcid.org/0000-0001-6341-7178>

Paul R. Brook <https://orcid.org/0000-0003-3053-6538>

Sarah Burke-Spolaor <https://orcid.org/0000-0003-4052-7838>

J. Andrew Casey-Clyde <https://orcid.org/0000-0002-5557-4007>

Maria Charisi <https://orcid.org/0000-0003-3579-2522>

Shami Chatterjee <https://orcid.org/0000-0002-2878-1502>

Tyler Cohen <https://orcid.org/0000-0001-7587-5483>

James M. Cordes <https://orcid.org/0000-0002-4049-1882>

Neil J. Cornish <https://orcid.org/0000-0002-7435-0869>

Fronefield Crawford <https://orcid.org/0000-0002-2578-0360>

H. Thankful Cromartie <https://orcid.org/0000-0002-6039-692X>

Kathryn Crowter <https://orcid.org/0000-0002-1529-5169>

Megan E. DeCesar <https://orcid.org/0000-0002-2185-1790>

Paul B. Demorest <https://orcid.org/0000-0002-6664-965X>

Timothy Dolch <https://orcid.org/0000-0001-8885-6388>

Elizabeth C. Ferrara <https://orcid.org/0000-0001-7828-7708>

William Fiore <https://orcid.org/0000-0001-5645-5336>

Emmanuel Fonseca <https://orcid.org/0000-0001-8384-5049>

Gabriel E. Freedman <https://orcid.org/0000-0001-7624-4616>

Emiko Gardiner <https://orcid.org/0000-0002-8857-613X>

Nate Garver-Daniels <https://orcid.org/0000-0001-6166-9646>

Peter A. Gentile <https://orcid.org/0000-0001-8158-683X>

Joseph Glaser <https://orcid.org/0000-0003-4090-9780>

Deborah C. Good <https://orcid.org/0000-0003-1884-348X>

Kayhan Gültekin <https://orcid.org/0000-0002-1146-0198>

Jeffrey S. Hazboun <https://orcid.org/0000-0003-2742-3321>

Ross J. Jennings <https://orcid.org/0000-0003-1082-2342>

Aaron D. Johnson <https://orcid.org/0000-0002-7445-8423>

Megan L. Jones <https://orcid.org/0000-0001-6607-3710>

Andrew R. Kaiser <https://orcid.org/0000-0002-3654-980X>

David L. Kaplan <https://orcid.org/0000-0001-6295-2881>

Luke Zoltan Kelley <https://orcid.org/0000-0002-6625-6450>

Matthew Kerr <https://orcid.org/0000-0002-0893-4073>

Joey S. Key <https://orcid.org/0000-0003-0123-7600>

Nima Laal <https://orcid.org/0000-0002-9197-7604>

Michael T. Lam <https://orcid.org/0000-0003-0721-651X>

William G. Lamb <https://orcid.org/0000-0003-1096-4156>

Natalia Lewandowska <https://orcid.org/0000-0003-0771-6581>

Tingting Liu <https://orcid.org/0000-0001-5766-4287>

Duncan R. Lorimer <https://orcid.org/0000-0003-1301-966X>

Jing Luo <https://orcid.org/0000-0001-5373-5914>

Ryan S. Lynch <https://orcid.org/0000-0001-5229-7430>

Chung-Pei Ma <https://orcid.org/0000-0002-4430-102X>

Dustin R. Madison <https://orcid.org/0000-0003-2285-0404>

Alexander McEwen <https://orcid.org/0000-0001-5481-7559>

James W. McKee <https://orcid.org/0000-0002-2885-8485>

Maura A. McLaughlin <https://orcid.org/0000-0001-7697-7422>

Natasha McMann <https://orcid.org/0000-0002-4642-1260>

Bradley W. Meyers <https://orcid.org/0000-0001-8845-1225>

Chiara M. F. Mingarelli <https://orcid.org/0000-0002-4307-1322>

Andrea Mitridate <https://orcid.org/0000-0003-2898-5844>

Cherry Ng <https://orcid.org/0000-0002-3616-5160>

David J. Nice <https://orcid.org/0000-0002-6709-2566>

Stella Koch Ocker <https://orcid.org/0000-0002-4941-5333>

Ken D. Olum <https://orcid.org/0000-0002-2027-3714>

Timothy T. Pennucci <https://orcid.org/0000-0001-5465-2889>

Benetge B. P. Perera <https://orcid.org/0000-0002-8509-5947>

Nihan S. Pol  <https://orcid.org/0000-0002-8826-1285>
 Henri A. Radovan  <https://orcid.org/0000-0002-2074-4360>
 Scott M. Ransom  <https://orcid.org/0000-0001-5799-9714>
 Paul S. Ray  <https://orcid.org/0000-0002-5297-5278>
 Joseph D. Romano  <https://orcid.org/0000-0003-4915-3246>
 Shashwat C. Sardesai  <https://orcid.org/0009-0006-5476-3603>
 Ann Schmiedekamp  <https://orcid.org/0000-0003-4391-936X>
 Carl Schmiedekamp  <https://orcid.org/0000-0002-1283-2184>
 Kai Schmitz  <https://orcid.org/0000-0003-2807-6472>
 Levi Schult  <https://orcid.org/0000-0001-6425-7807>
 Brent J. Shapiro-Albert  <https://orcid.org/0000-0002-7283-1124>
 Xavier Siemens  <https://orcid.org/0000-0002-7778-2990>
 Joseph Simon  <https://orcid.org/0000-0003-1407-6607>
 Magdalena S. Siwek  <https://orcid.org/0000-0002-1530-9778>
 Ingrid H. Stairs  <https://orcid.org/0000-0001-9784-8670>
 Daniel R. Stinebring  <https://orcid.org/0000-0002-1797-3277>
 Kevin Stovall  <https://orcid.org/0000-0002-7261-594X>
 Abhimanyu Susobhanan  <https://orcid.org/0000-0002-2820-0931>
 Joseph K. Swiggum  <https://orcid.org/0000-0002-1075-3837>
 Stephen R. Taylor  <https://orcid.org/0000-0001-8217-1599>
 Jacob E. Turner  <https://orcid.org/0000-0002-2451-7288>
 Caner Unal  <https://orcid.org/0000-0001-8800-0192>
 Michele Vallisneri  <https://orcid.org/0000-0002-4162-0033>
 Sarah J. Vigeland  <https://orcid.org/0000-0003-4700-9072>
 Haley M. Wahl  <https://orcid.org/0000-0001-9678-0299>
 Caitlin A. Witt  <https://orcid.org/0000-0002-6020-9274>
 Olivia Young  <https://orcid.org/0000-0002-0883-0688>

References

- Afzal, A., Agazie, G., Anumarlapudi, A., et al. 2023, *ApJL*, 951, L11
 Agazie, G., Alam, M. F., Anumarlapudi, A., et al. 2023a, *ApJL*, 951, L9
 Agazie, G., Anumarlapudi, A., Archibald, A. M., et al. 2023b, *ApJL*, 951, L8
 Agazie, G., Anumarlapudi, A., Archibald, A. M., et al. 2023c, *ApJL*, 951, L10
 Agazie, G., Anumarlapudi, A., Archibald, A. M., et al. 2023d, *ApJL*, 952, L37
 Ali-Haïmoud, Y., Smith, T. L., Mingarelli, C. M. F., et al. 2020, *PhRvD*, 102, 122005
 Ali-Haïmoud, Y., Smith, T. L., Mingarelli, C. M. F., et al. 2021, *PhRvD*, 103, 042009
 Allen, B. 2023, *PhRvD*, 107, 043018
 Allen, B., & Ottewill, A. C. 1997, *PhRvD*, 56, 545
 Allen, B., & Romano, J. D. 2023, *PhRvD*, 108, 043026
 Arzoumanian, Z., Baker, P. T., Blecha, L., et al. 2023, *ApJL*, 951, L28
 Arzoumanian, Z., Baker, P. T., Blumer, H., et al. 2021, *ApJL*, 923, L22
 Astropy Collaboration, Price-Whelan, A. M., Lim, P. L., et al. 2022, *ApJ*, 935, 167
 Bailes, M., Jameson, A., Abbate, F., et al. 2020, *PASA*, 37, e028
 Ballmer, S. W. 2006, *CQGra*, 23, S179
 Banagiri, S., Criswell, A., Kuan, T., et al. 2021, *MNRAS*, 507, 5451
 Bartolo, N., Bertacca, D., Caldwell, R., et al. 2022, *JCAP*, 2022, 009
 Bécsy, B., & Cornish, N. J. 2020, *CQGra*, 37, 135011
 Bécsy, B., Cornish, N. J., & Kelley, L. Z. 2022, *ApJ*, 941, 119
 Belgacem, E., & Kamionkowski, M. 2020, *PhRvD*, 102, 023004
 Bertacca, D., Ricciardone, A., Bellomo, N., et al. 2020, *PhRvD*, 101, 103513
 Biscoveanu, S., Talbot, C., Thrane, E., & Smith, R. 2020, *PhRvL*, 125, 241101
 Boyle, L., & Pen, U.-L. 2012, *PhRvD*, 86, 124028
 Chamberlin, S. J., Creighton, J. D. E., Siemens, X., et al. 2015, *PhRvD*, 91, 044048
 Chung, A. K.-W., Jenkins, A. C., Romano, J. D., & Sakellariadou, M. 2022, *PhRvD*, 106, 082005
 Contaldi, C. R., Pieroni, M., Renzini, A. I., et al. 2020, *PhRvD*, 102, 043502
 Cornish, N. J. 2001, *CQGra*, 18, 4277
 Cornish, N. J., & Sampson, L. 2016, *PhRvD*, 93, 104047
 Cornish, N. J., & Sesana, A. 2013, *CQGra*, 30, 224005
 Cornish, N. J., & van Haasteren, R. 2014, arXiv:1406.4511
 Cusin, G., & Tasinato, G. 2022, *JCAP*, 2022, 036
 Demorest, P. B., Ferdman, R. D., Gonzalez, M. E., et al. 2013, *ApJ*, 762, 94
 Detweiler, S. 1979, *ApJ*, 234, 1100
 Ellis, J., Siemens, X., & Chamberlin, S. 2012, arXiv:1210.5274
 Ellis, J. A., Vallisneri, M., Taylor, S. R., & Baker, P. T. 2020, ENTERPRISE: Enhanced Numerical Toolbox Enabling a Robust Pulsar Inference Suite, doi:10.5281/zenodo.4059815
 Ellis, J. A., & van Haasteren, R. 2017, ellis18/PTMCMCSampler: Official Release, v1.0.0, doi:10.5281/zenodo.1037579
 Essick, R., Farr, W. M., Fishbach, M., Holz, D. E., & Katsavounidis, E. 2023, *PhRvD*, 107, 043016
 Estabrook, F. B., & Wahlquist, H. D. 1975, *GReGr*, 6, 439
 Flanagan, E. E. 1993, *PhRvD*, 48, 2389
 Floden, E., Mandic, V., Matas, A., & Tsukada, L. 2022, *PhRvD*, 106, 023010
 Gair, J., Romano, J. D., Taylor, S., & Mingarelli, C. M. F. 2014, *PhRvD*, 90, 082001
 Górski, K. M., Hivon, E., Banday, A. J., et al. 2005, *ApJ*, 622, 759
 Harris, C. R., Millman, K. J., van der Walt, S. J., et al. 2020, *Natur*, 585, 357
 Hazboun, J. S., Mingarelli, C. M. F., & Lee, K. 2018, arXiv:1810.10527
 Hellinger, E. 1909, *JRAM*, 1909, 210
 Hellings, R. W., & Downs, G. S. 1983, *ApJL*, 265, L39
 Hobbs, G. 2013, *CQGra*, 30, 224007
 Hobbs, G., Archibald, A., Arzoumanian, Z., et al. 2010, *CQGra*, 27, 084013
 Hotinli, S. C., Kamionkowski, M., & Jaffe, A. H. 2019, *OJAp*, 2, 8
 Hunter, J. D. 2007, *CSE*, 9, 90
 Joshi, B. C., Arumugasamy, P., Bagchi, M., et al. 2018, *JapA*, 39, 51
 Kaiser, A. R., Pol, N. S., McLaughlin, M. A., et al. 2022, *ApJ*, 938, 115
 Kato, R., & Soda, J. 2016, *PhRvD*, 93, 062003
 Kluyver, T., Ragan-Kelley, B., Pérez, F., et al. 2016, in Positioning and Power in Academic Publishing: Players, Agents and Agendas, ed. F. Loizides & B. Schmidt (Amsterdam: IOS Press), 87
 Kramer, M., & Champion, D. J. 2013, *CQGra*, 30, 224009
 Levenberg, K. 1944, *QApMa*, 2, 164
 Liu, G.-C., & Ng, K.-W. 2022, *PhRvD*, 106, 064004
 Ivezic, Ž., Connelly, A. J., Vanderplas, J. T., & Gray, A. 2019, Statistics, Data Mining, and Machine Learning in Astronomy: A Practical Python Guide for the Analysis of Survey Data, Updated Edition (Princeton, NJ: Princeton Univ. Press),
 Mandic, V., Thrane, E., Giampanis, S., & Regimbau, T. 2012, *PhRvL*, 109, 171102
 Marquardt, D. W. 1963, *SIAP*, 11, 431
 Martinovic, K., Meyers, P. M., Sakellariadou, M., & Christensen, N. 2021, *PhRvD*, 103, 043023
 McLaughlin, M. A. 2013, *CQGra*, 30, 224008
 Meyers, P. M., Chatziioannou, K., Vallisneri, M., & Chua, A. J. K. 2023, doi:10.48550/arXiv.2306.05559
 Mingarelli, C. M. F., Lazio, T. J. W., Sesana, A., et al. 2017, *NatAs*, 1, 886
 Mingarelli, C. M. F., & Mingarelli, A. B. 2018, *JPhCo*, 2, 105002
 Mingarelli, C. M. F., & Sidery, T. 2014, *PhRvD*, 90, 062011
 Mingarelli, C. M. F., Sidery, T., Mandel, I., & Vecchio, A. 2013, *PhRvD*, 88, 062005
 Mitra, S., Dhurandhar, S., Souradeep, T., et al. 2008, *PhRvD*, 77, 042002
 Newville, M., Otten, R., Nelson, A., et al. 2021, lmfitt/lmfitt-py: v1.0.3, Zenodo, doi:10.5281/zenodo.5570790
 Ölmez, S., Mandic, V., & Siemens, X. 2012, *JCAP*, 2012, 009
 Parida, A., Mitra, S., & Jhingan, S. 2016, *JCAP*, 2016, 024
 Payne, E., Banagiri, S., Lasky, P. D., & Thrane, E. 2020, *PhRvD*, 102, 102004
 Perera, B. B. P., DeCesar, M. E., Demorest, P. B., et al. 2019, *MNRAS*, 490, 4666
 Phinney, E. S. 2001, arXiv:astro-ph/0108028
 Planck Collaboration, Aghanim, N., Akrami, Y., et al. 2020, *A&A*, 641, A1
 Pol, N., Taylor, S. R., & Romano, J. D. 2022, *ApJ*, 940, 173
 Pol, N. S., Taylor, S. R., Kelley, L. Z., et al. 2021, *ApJL*, 911, L34
 Ransom, S., Brazier, A., Chatterjee, S., et al. 2019, *BAAS*, 51, 195
 Renzini, A. I., & Contaldi, C. R. 2018, *MNRAS*, 481, 4650
 Romano, J. D., & Cornish, N. J. 2017, *LRR*, 20, 2
 Romano, J. D., Hazboun, J. S., Siemens, X., & Archibald, A. M. 2021, *PhRvD*, 103, 063027
 Sato-Polito, G., & Kamionkowski, M. 2022, *PhRvD*, 106, 023004
 Sato-Polito, G., & Kamionkowski, M. 2023, arXiv:2305.05690
 Sazhin, M. V. 1978, *SvA*, 22, 36

- Siemens, X., Ellis, J., Jenet, F., & Romano, J. D. 2013, *CQGra*, **30**, 224015
- Suresh, J., Agarwal, D., & Mitra, S. 2021, *PhRvD*, **104**, 102003
- Taylor, S. R., Baker, P. T., Hazboun, J. S., Simon, J. J., & Vigeland, S. J. 2018, *enterprise_extensions*, v2.4.3, https://github.com/nanograv/enterprise_extensions
- Taylor, S. R., & Gair, J. R. 2013, *PhRvD*, **88**, 084001
- Taylor, S. R., Lentati, L., Babak, S., et al. 2017, *PhRvD*, **95**, 042002
- Taylor, S. R., Mingarelli, C. M. F., Gair, J. R., et al. 2015, *PhRvL*, **115**, 041101
- Taylor, S. R., van Haasteren, R., & Sesana, A. 2020, *PhRvD*, **102**, 084039
- Thrane, E., Ballmer, S., Romano, J. D., et al. 2009, *PhRvD*, **80**, 122002
- Ungarelli, C., & Vecchio, A. 2001, *PhRvD*, **64**, 121501
- Valbusa Dall'Armi, L., Ricciardone, A., & Bertacca, D. 2022, *JCAP*, **2022**, 040
- Vallisneri, M., Meyers, P. M., Chatziioannou, K., & Chua, A. J. K. 2023, [arXiv:2306.05558](https://arxiv.org/abs/2306.05558)
- Vigeland, S. J., Islo, K., Taylor, S. R., & Ellis, J. A. 2018, *PhRvD*, **98**, 044003
- Virtanen, P., Gommers, R., Oliphant, T. E., et al. 2020, *NatMe*, **17**, 261
- Zonca, A., Singer, L. P., Lenz, D., et al. 2019, *JOSS*, **4**, 1298